Check for updates

Dual-molecule reciprocal doping strategy for cathode interfacial materials enables over 20.7% efficiency in organic solar cells

Chengcheng Xie,[a] Yuanpeng Xie, [ID] *[a] Longjun Fu,[a] Xiaxia Yang,[a] Nian Zhang,[a] Bo Xu,[a] Zhuo Wang,[a] Dianyong Tang, [ID] [c] Liming Ding, [ID] [d] Feng Liu [ID] *[b] and Menglan Lv*[a]

Solution-processable cathode interfacial materials (CIMs) in organic solar cells (OSCs) inherently suffer from limited conductivity and charge transfer capabilities, which in turn restrict device efficiency. In this study, we report a double-doped CIM, PDINN-CNT2N, which combines organic PDINN with aminated carbon nanotubes through a reciprocal doping strategy. This strategy leverages intramolecular self-doping and intermolecular reciprocal doping between the two components to markedly enhance the electron density and charge transport properties of the developed CIM. Simultaneously, the intermolecular interactions effectively optimize molecular assembly, thereby reinforcing the electron mobility within the films. OSCs utilizing the PDINN-CNT2N CIM demonstrate improved conductivity and electron mobility while reducing charge recombination. Consequently, OSCs based on binary D18:L8-BO achieve an efficiency of 20.05% with superior stability. The widespread applicability of this strategy is further confirmed across additional CNT2N-based CIMs and various active layer systems, significantly enhancing the efficiency to 20.72% (certified as 20.33%) in a ternary system. The study provides essential insights into molecular synergistic doping and presents a universal approach for designing high-performance CIMs that are suitable for scalable solution processing.

Broader context

Organic solar cells (OSCs) have recently surpassed their power conversion efficiency to over 20%, with cathode interfacial materials (CIMs) playing a central role in facilitating charge transport and reducing charge recombination. However, conventional solution-processable CIMs often suffer from limited conductivity and inefficient charge transport, restricting further performance improvements. Hybrid CIMs that combine a primary interfacial material with a secondary functional component offer improved charge transport through complementary electronic properties and synergistic interactions. Building on this concept, we developed a doping-based hybrid CIM by grafting amino groups onto carbon nanotubes (CNT2N) and integrating them with PDINN, thereby establishing a reciprocal doping strategy. Reciprocal electron donation between CNT2N and PDINN increases carrier density and conductivity, while pronounced supramolecular π–π stacking interactions independently promote ordered PDINN assemblies and epitaxial adsorption on CNT surfaces, enhancing molecular ordering and charge mobility. The coexistence of these two independent yet synergistic mechanisms creates multidimensional charge-transport networks, leading to accelerated charge extraction and reduced recombination. Devices employing PDINN-CNT2N hybrid CIMs achieved PCEs of 20.05% in the binary D18:L8-BO system and 20.72% in the ternary D18:L8-BO:BTP-eC9 system, demonstrating the broad applicability of this strategy for advancing high-performance OSCs.

[a] *Engineering Research Center for Energy Conversion and Storage Technology of Guizhou, School of Chemistry and Chemical Engineering, Guizhou University, Guiyang, P. R. China. E-mail: ypxie@gzu.edu.cn, mllv@gzu.edu.cn*

[b] *Frontiers Science Center for Transformative Molecules, In-situ Center for Physical Science, and Center of Hydrogen Science, School of Chemistry and Chemical Engineering, Shanghai Jiao Tong University, Shanghai, P. R. China. E-mail: fengliu82@sjtu.edu.cn*

[c] *Chongqing University of Arts and Sciences, Chongqing, P. R. China*

[d] *School of Chemical Engineering and Light Industry, Guangdong University of Technology, Guangzhou, P. R. China*

1. Introduction

Advances in photoactive materials through morphology control and device engineering have propelled the power conversion efficiency (PCE) of organic solar cells (OSCs) to over 20%.[1–5] The solution-processable organic cathode interfacial materials (CIMs),[6–14] which improve Ohmic contact and enhance charge extraction, play a pivotal role in achieving high device efficiency.[15–18] The perylene diimide (PDI)-based *n*-type

This journal is © The Royal Society of Chemistry 2026

Energy Environ. Sci., 2026, **19**, 2237–2245 | **2237**

semiconductors are important CIMs due to their efficiency in attaining an optimal energy-level alignment.[19–22] Nonetheless, PDI-based CIMs are limited by their intrinsic low carrier density, which limits their charge extraction capability.[23] Introducing polar groups can enhance the self-doping effect in CIMs, increasing conductivity to some extent, but still insufficient for high-efficiency devices.[24]

Recent advances in hybrid CIMs offer new strategies to enhance the doping effect by promoting interactions between components, including coordination bonds, hydrogen bonding, and π–π interactions.[25,26] Furthermore, intrinsic defects at the interface can be passivated, which boosts conductivity and thus enables highly efficient charge extraction.[27,28] As we have shown previously, low-dimensional carbon nanomaterials such as graphene and carbon nanotubes (CNTs) can be doped by polar group-functionalized PDI derivatives to significantly improve charge extraction rates.[29–31] These findings present a strategy to control the electronic state of CIMs through reciprocal doping, including PDI derivatives doping carbon nanomaterials and functional groups in carbon materials doping PDI derivatives. This strategy forms quadrupoles per reciprocal doping pair, generating multiple doped carriers and doubling the carrier density in CIMs.

Herein, we chemically grafted amino groups onto carbon nanotubes (CNT2N) and mixed them with PDINN to create reciprocal doping pairs. The amino groups in PDINN and CNT2N donate electrons to each other to induce doping, as confirmed by EPR, Raman and XPS analyses. The new molecular cluster enhances the dispersion of CNTs and processability. Supramolecular π–π interactions are observed, as seen from extended coherence lengths, suggesting that the π–π stacking-induced PDINN assemblies could be adsorbed on the CNT surface via epitaxy. Such an effect creates a network that facilitates charge transport. It should be noted that CNT2N and PDINN can self-dope mechanically. However, the existing intermolecular π–π stacking makes the molecules better intercalated, which contributes favorably to both carrier density and transport pathways. Consequently, the OSC using PDINN-CNT2N CIM achieved a high PCE of 20.05% in the binary D18:L8-BO system. This strategy shows broad applicability and yielded a champion PCE of 20.72% (certified as 20.33%) in the ternary D18:L8-BO:BTP-eC9 system, demonstrating its potential to overcome current interfacial limitations and advance the efficiencies of next-generation OSCs.

2. Results and discussion

2.1. Synthetic routes and characterization

The chemical structure of CNT2N is depicted in Fig. 1a. The synthetic route for the target CNT2N and its side-chain compound S2 is shown in Fig. S1. The related organic monomers were confirmed using ^{1}H NMR spectroscopy, with detailed reaction conditions provided in the SI. Fourier transform infrared (FTIR) analysis revealed distinct vibrational characteristics and alterations in peak positions and intensities (Fig. 1b),
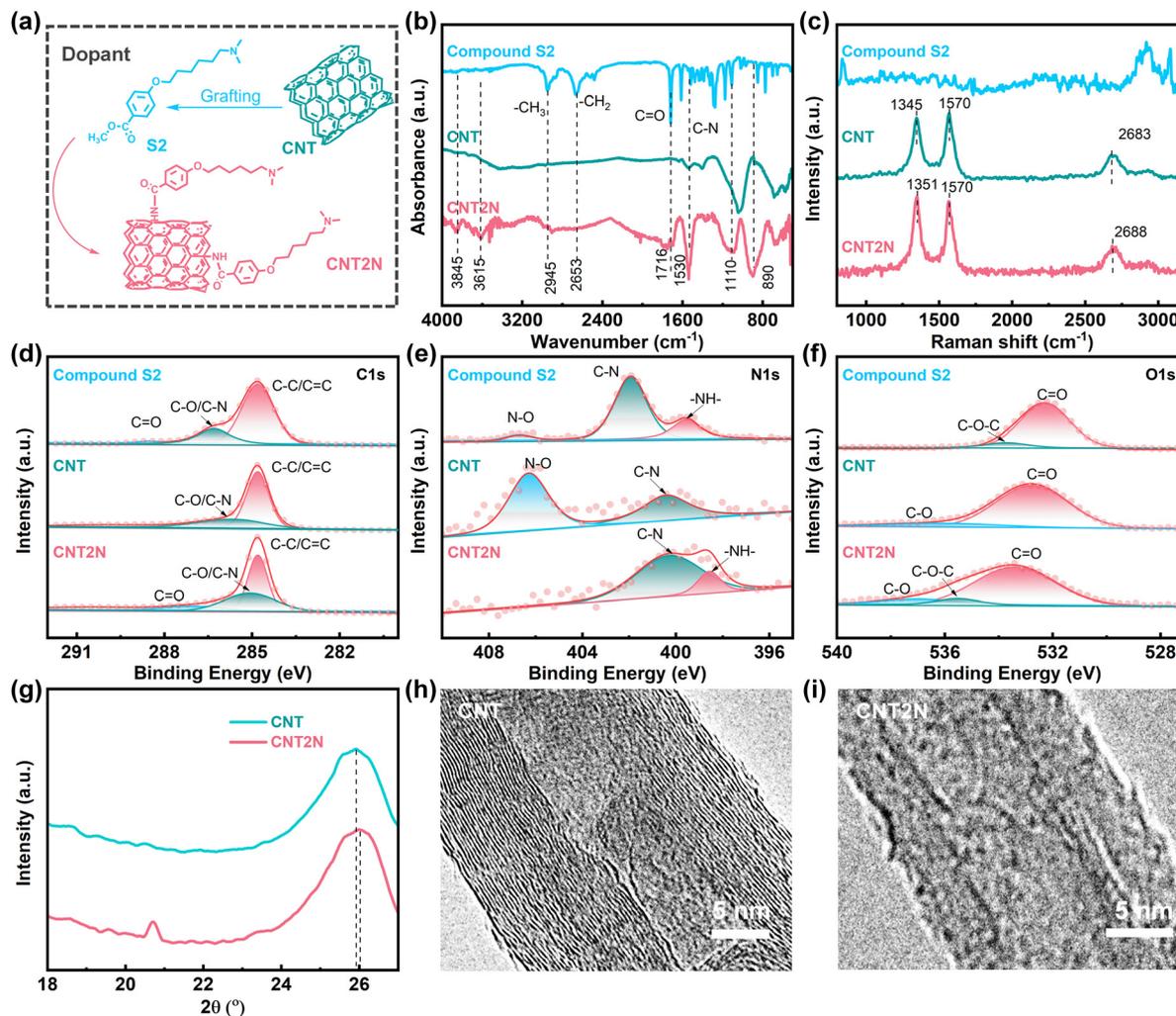
with CNT2N exhibiting characteristic absorptions associated with compound S2. Additionally, it shows extra bands at 1530, 1110, and 889 cm^{-1}, corresponding to the C–N stretching vibrations of amide and tertiary amino groups.[32] In the Raman spectrum, the D band shifts from 1345 to 1351 cm^{-1}, and there is an increase in the I_D/I_G ratio, signifying that covalent functionalization enhances structural disorder (Fig. 1c). These results signify the formation of essential chemical bonds and define the structural properties of CNT2N.

X-ray photoelectron spectroscopy (XPS) further provides detailed insights into surface chemical states. The binding energies for the key peaks, C 1s, N 1s, and O 1s are listed in Table S1. In the deconvoluted C 1s spectrum (Fig. 1d), the C–O/C–N and C=O peaks in CNT2N exhibit a shift to lower binding energies compared to compound S2 and CNT. This shift is more significant in the N 1s spectrum (Fig. 1e), where the C–N and N–H peaks exhibit shifts of 1.7 and 1.0 eV, respectively. In pristine CNTs, the N 1s peak arises from nitrogen species adsorbed from the air.[33] In the O 1s spectrum (Fig. 1f), CNT2N shows a shift to higher binding energy, accompanied by the emergence of a new C–O–C peak. The XPS spectral features and peak shifts further verify the successful synthesis of CNT2N, while the grafted amino groups enhance the surface electron density, thereby promoting interfacial charge transfer.[34] X-ray diffraction (XRD) patterns reveal a slight shift in the graphite peak of CNT2N from 25.9° to 26.1° (Fig. 1f), retaining a lattice structure similar to that of pristine CNTs (Fig. S2). Transmission electron microscopy (TEM) confirms that CNT2N maintains its hollow tubular shape despite reduced graphitic ordering (Fig. 1h and i).[35] These XRD and TEM analyses indicate that CNT2N retains its intrinsic conductive framework despite surface covalent functionalization.

2.2. Doping mechanisms and interaction behaviors

For the implementation of the hybrid CIM, the universal CIM PDINN involving specific dipolar groups was chosen as the host organic component and combined with CNT2N. The resulting mixture dissolved in methanol and underwent low-temperature ultrasonication, producing a stable PDINN-CNT2N suspension (Fig. S3). To understand the electronic structure changes of PDINN upon combination with CNT2N, density functional theory (DFT) calculations were subsequently conducted. As shown in Fig. 2a and Fig. S4, differential charge density maps were simulated for PDINN located outside and inside CNT2N. Three distinct charge transfer modes are revealed: (1) between the core of PDINN and CNT2N side chains, (2) between the PDINN side chains and the CNT2N outer tube wall, and (3) between the PDINN side chains and the CNT2N inner tube wall. In all three modes, pronounced charge delocalization between PDINN and CNT2N is observed. The differential charge densities (ΔCHG) of nitrogen-containing functional groups in PDINN and CNT2N were calculated and are listed in Table S2. An increase in charge density is observed for the nitrogen-containing groups on both PDINN and CNT2N surfaces. These findings theoretically confirm strong electronic delocalization and enhanced electron density between PDINN and CNT2N,

2238 | *Energy Environ. Sci.*, 2026, **19**, 2237–2245

This journal is © The Royal Society of Chemistry 2026

Fig. 1 (a) Schematic of CNT2N synthesis *via* the grafting of side-chain compound S2 onto CNT. (b) FT-IR spectra and (c) Raman spectra of compound S2, CNT and CNT2N. (d)–(f) High-resolution XPS spectra of C 1s, N 1s and O 1s for compound S2, CNT and CNT2N, respectively. (g) Magnified XRD patterns of CNT2N and CNT in the 2θ range of $18°$–$27°$. TEM images of (h) CNT and (i) CNT2N.
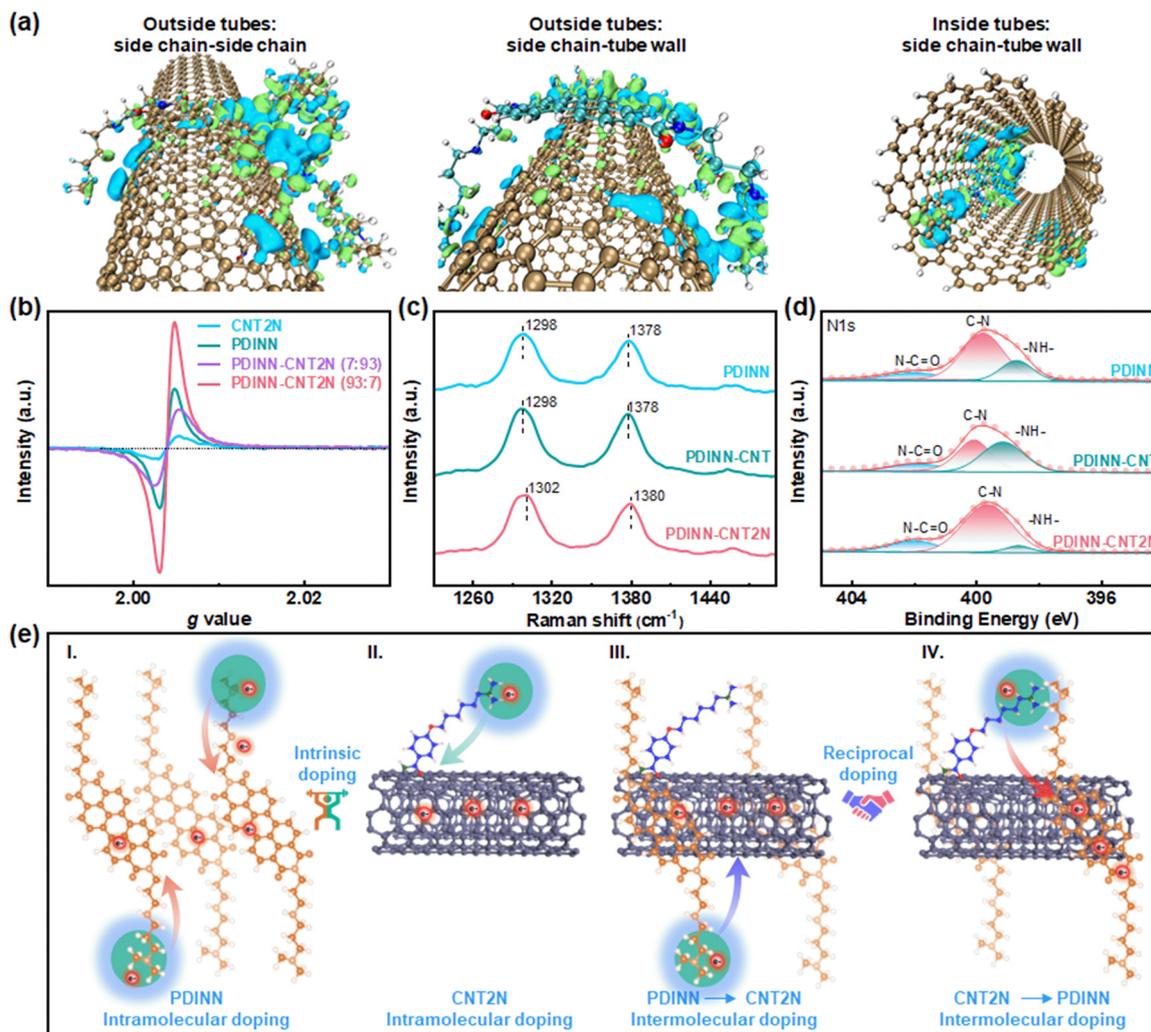
indicating reciprocal electronic doping effects that are expected to facilitate rapid charge transport.

Quantitative electron paramagnetic resonance (EPR) measurements were performed to investigate the doping effect between CNT2N and PDINN (Fig. 2b). Both CNT2N and PDINN display distinct EPR signals with a g-factor of 2.004, signifying self-doping within each molecule. Significantly, when PDINN and CNT2N are blended in a 7 : 93 mass ratio, there is a notable enhancement in the EPR signal compared to pure CNT2N. This indicates that PDINN effectively dopes CNT2N, promoting charge transfer from PDINN to CNT2N. Conversely, PDINN-CNT2N (93 : 7) shows the strongest EPR signal, suggesting that CNT2N effectively dopes PDINN, facilitating charge transfer from CNT2N to PDINN. The EPR findings confirm the existence of an interfacial reciprocal doping mechanism, resulting in a substantial enhancement of carrier concentration in the PDINN-CNT2N CIM, in line with the DFT results.

To comprehensively elucidate the reciprocal doping behavior, spectroscopic analyses were performed on the PDINN-CNT2N

hybrid CIM and two control samples (PDINN-CNT and pristine PDINN). In the FTIR spectra (Fig. S5), the C–N (1168 cm^{-1}) stretching peak of the PDINN-CNT2N CIM shifts downward by 3–6 cm^{-1} compared to the controls. Additionally, both the C–N and the C–H peaks (746–810 cm^{-1}) are significantly enhanced. The Raman spectra show blue shifts of 4 and 2 cm^{-1} for the PDI core peaks, which moved from $1298/1378 \text{ cm}^{-1}$ in PDINN to $1302/1380 \text{ cm}^{-1}$ in PDINN-CNT2N (Fig. 2c). In the deconvoluted C 1s spectra (Fig. S6), the C–C/C═C peak of PDINN-CNT2N shows a 0.1 eV decrease in binding energy compared to PDINN. Similarly, in the deconvoluted N 1s spectra (Fig. 2d), the intensity of the C–N peak increases, while the –NH– peak decreases, and both peaks shift to lower binding energies (Table S1). These concurrent spectral shifts reveal a redistribution and overall enrichment of electronic density in the PDINN-CNT2N system, indicative of pronounced electronic delocalization and charge transfer.[36] Such modifications alter the bond strength and local electronic structure, demonstrating that CNT2N enables more effective molecular doping of PDINN, in

This journal is © The Royal Society of Chemistry 2026

Energy Environ. Sci., 2026, **19**, 2237–2245 | **2239**

Fig. 2 (a) Simulated differential charge density maps illustrating the three distinct charge transfer modes between PDINN and CNT2N. (b) EPR spectra, where PDINN-CNT2N (7 : 93) denotes a composition with 7 wt% PDINN, and PDINN-CNT2N (93 : 7) denotes a composition with 7 wt% CNT2N. (c) Raman spectra and (d) high-resolution XPS spectra of N 1s for the PDINN, PDINN-CNT and PDINN-CNT2N films. (e) Schematic of the CIM reciprocal doping mechanism.

agreement with the enhanced charge-transfer characteristics evidenced by the EPR results.

To sum up, Fig. 2e illustrates a multilevel doping mechanism that includes four doping types: (I) self-doping of PDINN, (II) self-doping of CNT2N, (III) intermolecular reciprocal doping from PDINN to CNT2N, and (IV) intermolecular reciprocal doping from CNT2N to PDINN. These four doping mechanisms support bidirectional charge transfer between PDINN and CNT2N, offering multiple pathways for efficient charge transport. Consistent with this multilevel doping-induced enhancement in charge transport, the PDINN-CNT2N film exhibited a conductivity of 2.35×10^{-5} S cm^{-1} (Fig. S7a), surpassing that of pristine PDINN (1.24×10^{-5} S cm^{-1}).

Time-resolved *in situ* absorption spectroscopy was employed to monitor the film formation kinetics (Fig. S8). Compared with the control samples, the PDINN-CNT2N film exhibits a markedly shorter aggregation stage duration (0.09 s), indicating accelerated film formation kinetics. The selective absorption

spectra reveal a pronounced enhancement of the 0–0 transition for PDINN-CNT2N during the solution-to-film transition, suggesting stronger pre-aggregation driven by intermolecular interactions. This behavior is attributed to intensified intermolecular interactions, with CNT2N likely serving as nucleation centers that promote rapid aggregation.

In order to elucidate the influence of interfacial interactions between PDINN and CNT2N on molecular aggregation, grazing-incidence wide-angle X-ray scattering (GIWAXS) measurements were performed (Fig. 3a–c). All three films demonstrated an edge-on molecular orientation, as evidenced by the (100) and (010) peaks observed in the out-of-plane (OOP) and in-plane (IP) directions, respectively. Compared with the other two control samples, the PDINN-CNT2N film displayed strong diffraction rings with evident OOP peaks, which can be attributed to the ordered stacking of the PDI core and the PDINN side chains. Such enhanced crystallinity induced by CNT2N incorporation is expected to promote more efficient charge transport.[37,38]
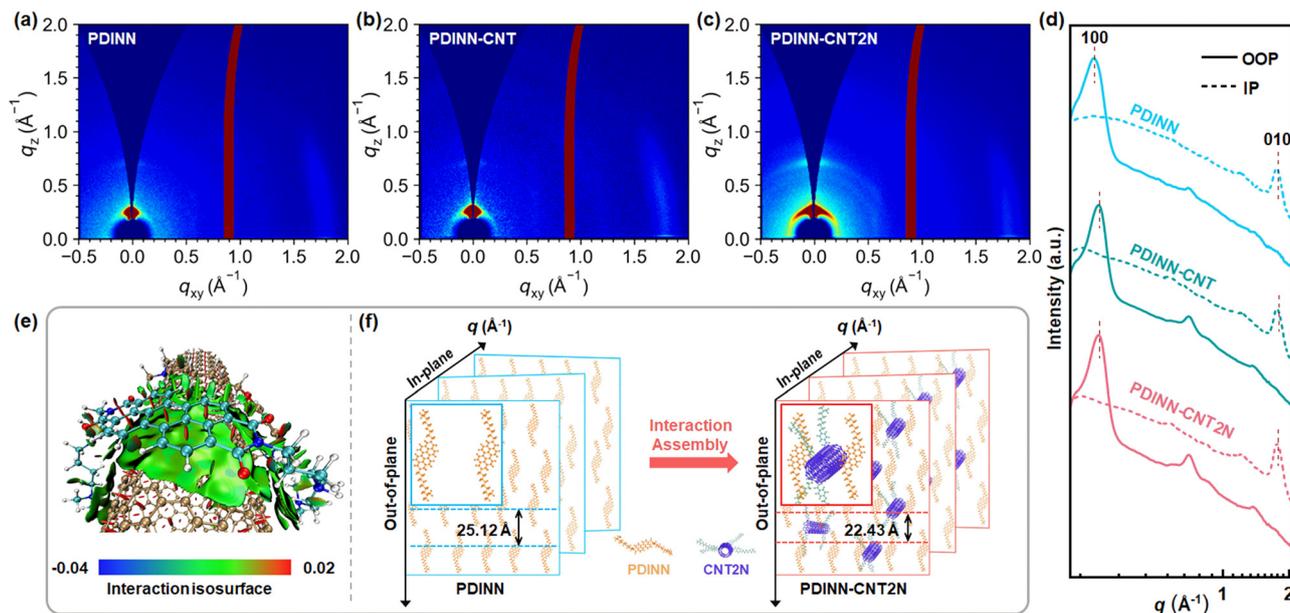
Fig. 3 (a)–(c) 2D GIWAXS patterns of the PDINN, PDINN-CNT, and PDINN-CNT2N films, respectively. (d) Corresponding IP and OOP line-cut profiles. (e) Simulated interaction between PDINN and CNT2N. (f) Schematic of the molecular stacking of the developed CIM.

The corresponding line-cut profiles are presented in Fig. 3d. Calculations of the π–π stacking distance (d-spacing) and crystalline coherence length (CCL) are summarized in Table S3. For PDINN-CNT2N, the CCL of the (010) peak in the IP direction increased from 8.79 to 11.32 Å, with a d-spacing of 3.53 Å. In the OOP direction, the (100) peak exhibited a CCL increase from 24.77 to 36.21 Å, accompanied by a decrease in d-spacing from 25.12 to 22.43 Å. These improvements demonstrate that the PDINN-CNT2N films possess denser stacking and more ordered molecular packing along both directions.

To investigate the origin of this enhancement, intermolecular interaction simulations were performed with the interaction region indicator (IRI) spatial function.[39] As shown in Fig. 3e and Fig. S9, the green-to-reddish regions between the tube wall of CNT2N and the benzene rings of PDINN confirm the presence of π–π stacking interactions. Moreover, UV-Vis measurements show a red-shifted absorption edge for PDINN-CNT2N relative to the controls (Fig. S10), indicating stronger intermolecular orbital coupling due to enhanced interactions and further supporting the presence of π–π stacking. Therefore, in combination with the GIWAXS results, we propose that upon CNT2N incorporation, π–π stacking interactions between CNT2N and PDINN effectively induce PDINN assembly, with PDINN adsorbing onto the CNT2N tube walls to form more ordered stacking with an increased CCL value (Fig. 3f). In addition, the presence of CNT2N side chains promotes tighter OOP packing, leading to reduced spacing. This interaction-driven assembly establishes a network that facilitates charge transport and enhances electron mobility. Corresponding to the enhanced structural order and molecular assembly, PDINN-CNT2N films exhibited an electron mobility of 8.01×10^{-4} cm^2 V^{-1} s^{-1} (Fig. S7b), markedly higher than that of pristine PDINN (2.13×10^{-4} cm^2 V^{-1} s^{-1}), demonstrating the beneficial effect of CNT2N incorporation on electron mobility.

2.3. Device performance

To assess the impact of the CNT2N reciprocal doping strategy on device performance, a series of OSCs with an indium tin oxide (ITO)/2PAThCz/PM6:L8-BO/CIMs/Ag architecture were fabricated, where 2PAThCz is derived from our recent work.[40] The chemical structures of the materials employed in this study are illustrated in Fig. S11. The detailed optimization processes are described in the Supporting Information (Fig. S12 and Table S4). The current density–voltage (J–V) characteristics of the devices are illustrated in Fig. 4a, with key parameters detailed in Table 1. The leading device, utilizing a PDINN-CNT2N CIM and PM6:L8-BO active layer, achieved a PCE of 19.50%, with an open-circuit voltage (V_{oc}) of 0.889 V, a short-circuit current density (J_{sc}) of 27.44 mA cm^{-2}, and a fill factor (FF) of 79.96%, surpassing the benchmark devices based on PDINN-CNT (19.08%) and unmodified PDINN (18.71%). Ultraviolet photoelectron spectroscopy (UPS) and UV-Vis measurements revealed that PDINN-CNT2N has a lowest unoccupied molecular orbital (LUMO) of −3.34 eV, and a work function of −3.53 eV (Fig. S13–S15 and Table S5). Compared with the two controls, these shallower levels facilitate electron transport and charge extraction,[14] supporting the improvement in J_{sc} and FF.

In subsequent evaluations, the compatibility of PDINN-CNT2N as a CIM was tested in the D18:L8-BO system (Fig. S16). The resulting device achieved a PCE of 20.05%, with an impressive FF exceeding 81.46%, outperforming devices based on PDINN-CNT (19.66%) and pristine PDINN (19.37%). To demonstrate the broad application of the reciprocal doping strategy, we further examined the performance of CNT2N combined with another electron-rich organic CIM, PNDIT-
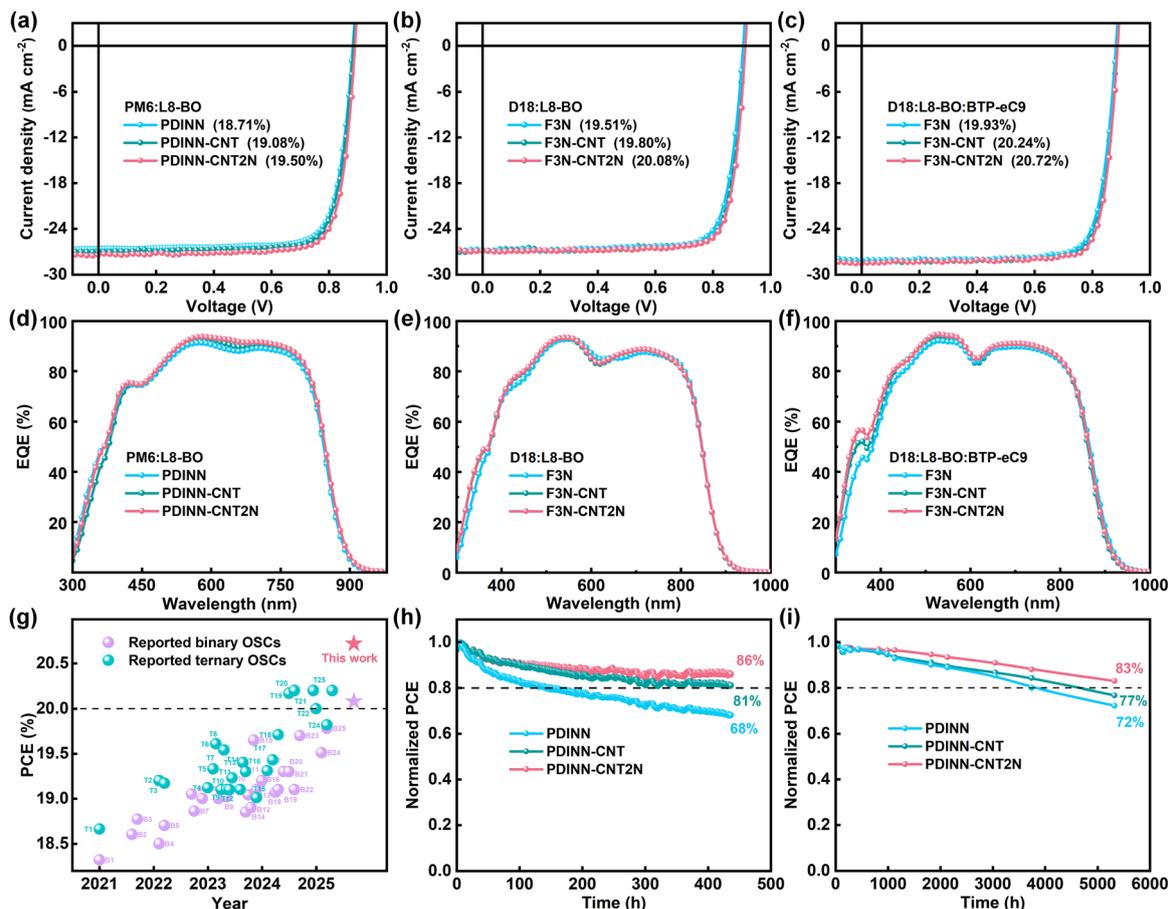
This journal is © The Royal Society of Chemistry 2026

Energy Environ. Sci., 2026, **19**, 2237–2245 | **2241**

Fig. 4 (a) J–V curves of OSCs based on PM6:L8-BO using the PDINN-CNT2N, PDINN-CNT, and PDINN CIMs. J–V curves of OSCs based on (b) D18:L8-BO and (c) D18:L8-BO:BTP-eC9 using the F3N-CNT2N, F3N-CNT, and F3N CIMs. Corresponding EQE spectra of OSCs based on (d) PM6:L8-BO, (e) D18:L8-BO, and (f) D18:L8-BO:BTP-eC9 with different CIMs. (g) Reported PCE statistics of OSCs in recent years. (h) Operational stability (in air) and (i) storage stability (in nitrogen) of devices based on the PDINN-CNT2N, PDINN-CNT, and PDINN CIMs.

Table 1   Photovoltaic parameters of devices with different active layers and CIMs

CIMs[a]	Active layer	V_{oc} [V]	J_{sc} [mA cm^{-2}]	J_{EQE}[b] [mA cm^{-2}]	FF [%]	PCE[c] [%]
PDINN	PM6:L8-BO	0.884	26.61	25.82	79.55	18.71 (18.29 ± 0.20)
PDINN-CNT		0.885	27.06	26.20	79.67	19.08 (18.63 ± 0.23)
PDINN-CNT2N		0.889	27.44	26.59	79.96	19.50 (19.17 ± 0.20)
PDINN	D18:L8-BO	0.897	26.85	25.99	80.45	19.37 (19.11 ± 0.17)
PDINN-CNT		0.902	26.91	26.08	80.98	19.66 (19.28 ± 0.18)
PDINN-CNT2N		0.905	27.19	26.32	81.46	20.05 (19.71 ± 0.19)
F3N	D18:L8-BO	0.904	26.82	25.94	80.47	19.54 (19.11 ± 0.22)
F3N-CNT		0.905	26.88	26.01	81.38	19.80 (19.60 ± 0.20)
F3N-CNT2N		0.911	26.90	26.10	81.88	20.08 (19.83 ± 0.15)
F3N	D18:L8-BO:BTP-eC9	0.882	28.14	27.19	80.32	19.93 (19.65 ± 0.21)
F3N-CNT		0.884	28.21	27.35	81.16	20.24 (19.99 ± 0.20)
F3N-CNT2N		0.888	28.55	27.75	81.72	20.72 (20.32 ± 0.21)

[a] Both CNT and CNT2N were doped into PDINN and F3N at a ratio of 7 wt%. [b] J_{EQE} was calculated from the EQE spectra. [c] Average PCEs with standard deviations were calculated from 10 individual devices. Detailed photovoltaic parameters are summarized in Tables S6–S21.

F3N (referred to as F3N).[41] As shown in the J–V curves of Fig. 4b, the D18:L8-BO system with a F3N-CNT2N CIM achieved a PCE of 20.08%, surpassing the performance of devices using F3N (Table 1). Notably, using D18:L8-BO:BTP-eC9 as the ternary active layer enhanced the device efficiency to 20.72% (Fig. 4c),

marking it as one of the highest PCEs reported for OSCs (Fig. 4g and Tables S22 and S23). This optimal device obtained a certified PCE of 20.33% subject to the calibration procedures of the National center of inspection on solar photovoltaic products quality (Fig. S17). The external quantum efficiency

(EQE) measurements of these different systems were consistent with the J_{sc} values obtained from J–V measurements, with discrepancies within 5% (Fig. 4d–f). PCE statistical analysis further emphasizes the marked improvement from single-component organic CIMs to CNT2N-based hybrid CIMs, suggesting enhanced device reliability (Fig. S18).

In addition, the stability of PDINN-CNT2N CIM-based devices was assessed and demonstrated superior performance compared to devices utilizing PDINN and PDINN-CNT. With a PM6:L8-BO active layer, the PDINN-CNT2N devices showed enhanced photostability under continuous LED light in ambient air (Fig. 4h), retaining 86% of their initial PCE after 440 hours and demonstrating a longer operational lifetime compared to the reference devices (Fig. S19). When stored in nitrogen for over 5300 hours, the PDINN-CNT2N devices preserved 83% of their starting efficiency (Fig. 4i). This enhanced stability is ascribed to the inherent robustness of the inorganic CNT2N component, reinforced intermolecular interactions, and stable multidimensional charge transport pathways.

2.4. Device physics

The study explored carrier dynamics and charge transport behavior in the devices through comprehensive electrical and optical assessments, with key parameters outlined in Table S24. Mott–Schottky analysis (Fig. 5a) revealed a notable increase in the built-in voltage (V_{bi}), rising from 0.593 V in the original PDINN device to 0.637 V in the PDINN-CNT2N CIM. This improvement supports efficient charge separation and directional transport.[42] Additionally, electrochemical impedance spectroscopy (Fig. 5b), performed in the dark at V_{bi}, showed a consistent decrease in series resistance (R_s) across the three

CIMs, following the order: R_s (PDINN-CNT2N) < R_s (PDINN-CNT) < R_s (PDINN). The reduction in R_s enhances carrier transport and minimizes trap-assisted recombination.[43,44] To delve deeper into charge transport behavior, we utilized the space-charge-limited current (SCLC) method with an electron-only device structured as ITO/ZnO/PM6:L8-BO/CIMs/Ag (Fig. 5c). The PDINN-CNT device exhibited electron mobility (μ_e) similar to that of standard PDINN. In contrast, the PDINN-CNT2N CIM displayed a higher μ_e of 1.04×10^{-4} cm^2 V^{-1} s^{-1}. This advancement promotes swifter charge diffusion and mitigates space-charge buildup.[45] Time-resolved photoluminescence (TRPL) measurements were performed (Fig. S20). The photoluminescence lifetime of the PM6/PDINN-CNT2N bilayer film (0.29 ns) is significantly shorter than those of the PM6/PDINN (0.38 ns) and PM6/PDINN-CNT (0.34 ns) films. This accelerated fluorescence quenching indicates enhanced charge extraction by PDINN-CNT2N CIM, which can be attributed to improved charge transport.

The study explored the relationship between light intensity (P_{light}) and both V_{oc} and J_{sc} to gain insights into recombination dynamics (Fig. S21).[46] In devices based on PDINN-CNT2N, the V_{oc} dependency on P_{light} exhibited the lowest slope of 1.09 kT q^{-1}, indicating a more effective suppression of trap-assisted recombination compared to PDINN-CNT (1.14 kT q^{-1}) and PDINN (1.12 kT q^{-1}) devices. Correspondingly, the J_{sc}–P_{light} relationship resulted in an α value of 0.999 for PDINN-CNT2N, higher than those for PDINN-CNT (0.996) and PDINN (0.991). This suggests a reduction in bimolecular recombination and enhanced charge extraction efficiency. Further, the kinetics of charge generation and dissociation were investigated by examining the dependence of photocurrent density (J_{ph}) on effective
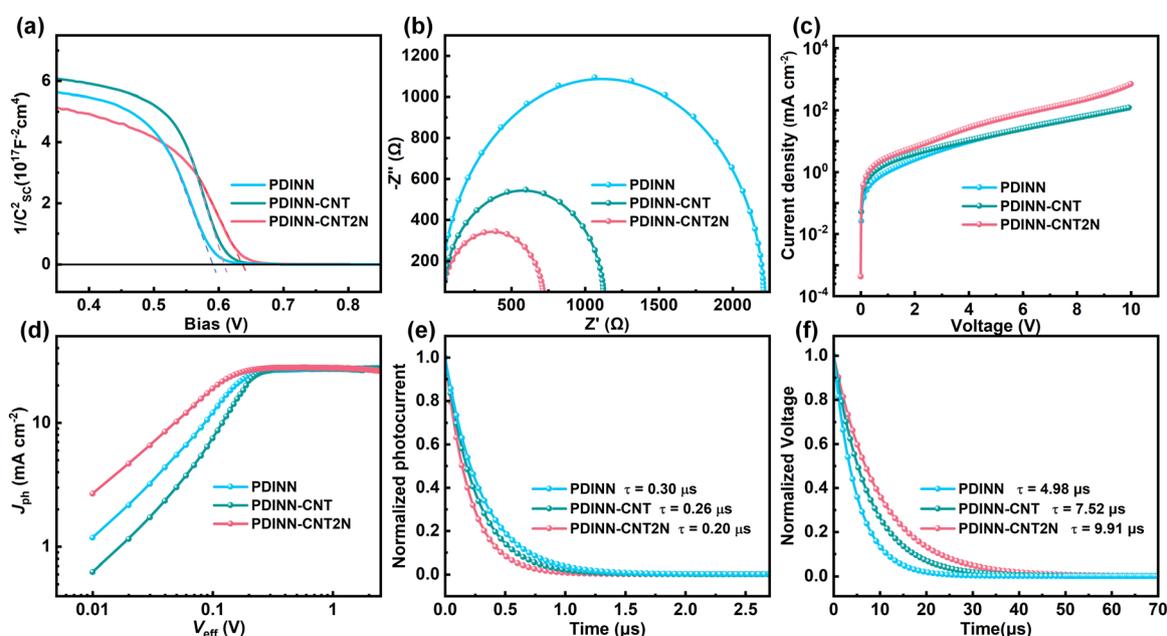

Fig. 5 (a) Mott–Schottky analysis of devices processed with various CIMs. (b) Impedance response of devices processed with various CIMs. The solid lines are the fitting results. (c) Electron mobility of the three CIMs evaluated using electron-only devices. (d) Photocurrent density (J_{ph}) plotted against effective bias (V_{eff}) for devices processed with various CIMs. (e) TPC and (f) TPV curves for the reference and doped PDINN-based devices.

This journal is © The Royal Society of Chemistry 2026

Energy Environ. Sci., 2026, **19**, 2237–2245 | **2243**

voltage (V_{eff}) (Fig. 5d), from which the exciton dissociation probability (P_{diss}) and charge collection efficiency (P_{coll}) were determined. The device incorporating the PDINN-CNT2N CIM outperformed others, with a P_{diss} of 99.28% and a P_{coll} of 92.00%, compared to PDINN-CNT (P_{diss}: 98.27%, P_{coll}: 90.41%) and pristine PDINN (P_{diss}: 99.18%, P_{coll}: 90.13%). This suggests that the CNT2N-doped device more effectively facilitates exciton dissociation and charge extraction at the interface. Further evidence from transient photocurrent (TPC) and transient photovoltage (TPV) measurements shows that the PDINN-CNT2N device boasts the shortest charge extraction time of 0.20 μs and the longest carrier lifetime of 9.91 μs, outperforming PDINN-CNT (0.26 μs, 7.52 μs) and pristine PDINN (0.30 μs, 4.98 μs), as indicated in Fig. 5e and f. Electroluminescence external quantum efficiency (EQE_{EL}) measurements indicate that CIMs based on PDINN-CNT2N exhibit higher EQE_{EL} (Fig. S22). These results suggest that PDINN-CNT2N not only promotes enhanced interfacial molecular ordering and stacking, but also facilitates efficient charge transport while suppressing trap-assisted recombination. Collectively, these improvements result in notably increased device efficiency and stability, underscoring the promise of this interfacial design in the development of high-performance organic photovoltaic devices.

3. Conclusion

In conclusion, we developed a novel double-doped hybrid CIM, PDINN-CNT2N, which effectively enhances the performance of OSCs through a dual-molecule reciprocal doping strategy. This innovative approach involves intramolecular self-doping within each component and intermolecular doping between different components, resulting in a robust hybrid material with high electron density, which significantly enhances conductivity. Moreover, strong interactions between CNT2N and PDINN facilitate the cooperative assembly of PDINN molecules, leading to hybrid CIM films with not only improved crystallinity but also a percolating charge transport network, collectively contributing to excellent charge mobility. These performance enhancements enable efficient charge extraction with minimal recombination losses. Binary OSCs using PDINN-CNT2N with PM6:L8-BO and D18:L8-BO achieved PCEs of 19.50% and 20.05%, respectively, with FF above 81.46% and outstanding stability. The dual-molecule reciprocal doping strategy has proven effective when utilized in various hybrid CIMs across different OSC types. Remarkably, its application to the F3N-CNT2N CIM in a ternary system yielded a PCE of 20.72%. This study underscores a promising approach for creating high-performance hybrid CIMs, paving the way for future advancements in efficient OSCs.

Author contributions

C. Xie conducted material synthesis, data collection, and manuscript preparation. C. Xie and X. Yang carried out device fabrication. L. Fu performed the GIWAXS and stability measurements. N. Zhang and B. Xu supported material synthesis. Z. Wang assisted in revising the manuscript. Y. Xie contributed to data presentation and manuscript revision. D. Tang and L. Ding contributed to data presentation and theoretical calculations. F. Liu and M. Lv contributed to conceptualization, result discussions, manuscript revision, and overall project supervision.

Conflicts of interest

There are no conflicts to declare.

Data availability

The data supporting this article have been included as part of the supplementary information (SI). Supplementary information is available. See DOI: https://doi.org/10.1039/d5ee06226h.

Acknowledgements

References

1 Z. Zheng, J. Wang, P. Bi, J. Ren, Y. Wang, Y. Yang, X. Liu, S. Zhang and J. Hou, *Joule*, 2022, **6**, 171–184.

2 S. Guan, Y. Li, C. Xu, N. Yin, C. Xu, C. Wang, M. Wang, Y. Xu, Q. Chen, D. Wang, L. Zuo and H. Chen, *Adv. Mater.*, 2024, **36**, 2400342.

3 C. Li, J. Song, H. Lai, H. Zhang, R. Zhou, J. Xu, H. Huang, L. Liu, J. Gao, Y. Li, M. H. Jee, Z. Zheng, S. Liu, J. Yan, X.-K. Chen, Z. Tang, C. Zhang, H. Y. Woo, F. He, F. Gao, H. Yan and Y. Sun, *Nat. Mater.*, 2025, **24**, 433–443.

4 H. Mou, Y. Yin, H. Chen, J. Xu, J. Ding, C. Ju, J. Zhu, Y. Wang, W. Chen, G. Xu, T. Zhang, J. Li, Y. Li and Y. Li, *J. Am. Chem. Soc.*, 2025, **147**, 21241–21251.

5 X. Duan, J. Song, J. Zhang, J. Zhuang, J. Deng, X. Wang, G. Dai, B. Song, J. Qiao, X. Hao, J. Zhang, R. Yang, G. Lu, F. Liu and Y. Sun, *Adv. Mater.*, 2025, **37**, 2503510.

6 N. Ahmad, H. Zhou, P. Fan and G. Liang, *EcoMat*, 2022, **4**, e12156.

7 D. W. Zhao, P. Liu, X. W. Sun, S. T. Tan, L. Ke and A. K. K. Kyaw, *Appl. Phys. Lett.*, 2009, **95**, 153304.

2244 | *Energy Environ. Sci.*, 2026, **19**, 2237–2245

This journal is © The Royal Society of Chemistry 2026

8 F. Huang, H. Wu, D. Wang, W. Yang and Y. Cao, *Chem. Mater.*, 2004, **16**, 708–716.

9 Y. Zhou, C. Fuentes-Hernandez, J. Shim, J. Meyer, A. J. Giordano, H. Li, P. Winget, T. Papadopoulos, H. Cheun and J. Kim, *Science*, 2012, **336**, 327–332.

10 X. H. Ouyang, R. X. Peng, L. Ai, X. Y. Zhang and Z. Y. Ge, *Nat. Photonics*, 2015, **9**, 520–524.

11 Z. A. Page, Y. Liu, V. V. Duzhko, T. P. Russell and T. Emrick, *Science*, 2014, **346**, 441–444.

12 Q. Kang, L. Ye, B. Xu, C. An, S. J. Stuard, S. Zhang, H. Yao, H. Ade and J. Hou, *Joule*, 2019, **3**, 227–239.

13 Y. Yu, J. Wang, Y. Cui, Z. Chen, T. Zhang, Y. Xiao, W. Wang, J. Wang, X. T. Hao and J. Hou, *J. Am. Chem. Soc.*, 2024, **146**, 8697–8705.

14 Y. Yu, J. Wang, Z. Chen, Y. Xiao, Z. Fu, T. Zhang, H. Yuan, X.-T. Hao, L. Ye, Y. Cui and J. Hou, *Sci. China: Chem.*, 2024, **67**, 4194–4201.

15 M. Du, X. Li, C. Mu, B. Zhou, P. Cong, H. Liu, A. Tang, Y. Liu and E. Zhou, *Adv. Funct. Mater.*, 2024, **34**, 2402974.

16 W. Kong, J. Wang, Y. Hu, N. Cui, C. Yan, X. Cai and P. Cheng, *Angew. Chem., Int. Ed.*, 2023, **62**, e202307622.

17 M. Günther, N. Kazerouni, D. Blätte, J. D. Perea, B. C. Thompson and T. Ameri, *Nat. Rev. Mater.*, 2023, **8**, 456–471.

18 X. Zhang, H. Zhang, Y. Li, S. U. Zafar, S. Yang, J. Chen, H. Zhou and Y. Zhang, *Adv. Funct. Mater.*, 2022, **32**, 2205398.

19 Z.-G. Zhang, B. Qi, Z. Jin, D. Chi, Z. Qi, Y. Li and J. Wang, *Energy Environ. Sci.*, 2014, **7**, 1966.

20 J. Yao, B. Qiu, Z. G. Zhang, L. Xue, R. Wang, C. Zhang, S. Chen, Q. Zhou, C. Sun, C. Yang, M. Xiao, L. Meng and Y. Li, *Nat. Commun.*, 2020, **11**, 2726.

21 X. Wang, Q. Liang, A. Zhang, N. Wei, H. Jiang, Y. Cheng, H. Fang, S. Li, H. Lu, W. Li and Z. Bo, *J. Am. Chem. Soc.*, 2025, **147**, 9261–9272.

22 K. Zhong, J. Deng, R. Zeng, J. Xu, Z. Yuan, C. Wang, L. Li, J. Liu, X. Zhao, Y. Hu, L. Chen and F. Liu, *Adv. Funct. Mater.*, 2024, **35**, 2414822.

23 J. Yao, Q. Chen, C. Zhang, Z. G. Zhang and Y. Li, *SusMat*, 2022, **2**, 243–263.

24 X. Song, Y. Song, H. Xu, S. Gao, Y. Wang, J. Li, J. Hai, W. Liu and W. Zhu, *Adv. Energy Mater.*, 2022, **13**, 2203009.

25 Y. Li, Z. Zhang, X. Han, T. Li and Y. Lin, *CCS Chem.*, 2022, **4**, 1087–1097.

26 H. Yang, W. Zhang, X. Li, Y. Yuan, Y. Wu, X. Xiong, C. Cui and Y. Li, *Angew. Chem., Int. Ed.*, 2025, **64**, e202507294.

27 Y. Zheng, J. Zhao, H. Li, M. Zhang, Z. Zhao, Y. Li, C. Zhu, A. Liang, Z. Wang, S. Xu and Z. Kan, *Mater. Sci. Eng., R*, 2025, **165**, 101007.

28 C. Li, Y. Cai, P. Hu, T. Liu, L. Zhu, R. Zeng, F. Han, M. Zhang, M. Zhang, J. Lv, Y. Ma, D. Han, M. Zhang, Q. Lin, J. Xu, N. Yu, J. Qiao, J. Wang, X. Zhang, J. Xia, Z. Tang, L. Ye, X. Li, Z. Xu, X. Hao, Q. Peng, F. Liu, L. Guo and H. Huang, *Nat. Mater.*, 2025, **24**, 1626–1634.

29 F. Pan, C. Sun, Y. Li, D. Tang, Y. Zou, X. Li, S. Bai, X. Wei, M. Lv, X. Chen and Y. Li, *Energy Environ. Sci.*, 2019, **12**, 3400–3411.

30 F. Pan, S. Bai, S. Liu, D. Tang, X. Wei, X. Chen, M. Lv and Y. Li, *Sci. China Chem.*, 2021, **64**, 565–575.

31 F. Pan, S. Bai, X. Wei, Y. Li, D. Tang, X. Chen, M. Lv and Y. Li, *Sci. China Mater.*, 2020, **64**, 277–287.

32 K. I. Hadjiivanov, D. A. Panayotov, M. Y. Mihaylov, E. Z. Ivanova, K. K. Chakarova, S. M. Andonova and N. L. Drenchev, *Chem. Rev.*, 2021, **121**, 1286–1424.

33 N. Hellgren, R. T. Haasch, S. Schmidt, L. Hultman and I. Petrov, *Carbon*, 2016, **108**, 242–252.

34 L. Lu, X. Liu, Y. Sun, S. Wang, J. Liu, S. Ge, T. Wei, H. Zhang, J. Su and Y. Zhang, *Adv. Mater.*, 2024, **36**, 2308748.

35 K. Jiang, S. Back, A. J. Akey, C. Xia, Y. Hu, W. Liang, D. Schaak, E. Stavitski, J. K. Norskov, S. Siahrostami and H. Wang, *Nat. Commun.*, 2019, **10**, 3997.

36 G. Li, Y.-Y. Zhang, Q. Li, C. Wang, Y. Yu, B. Zhang, H.-S. Hu, W. Zhang, D. Dai, G. Wu, D. H. Zhang, J. Li, X. Yang and L. Jiang, *Nat. Commun.*, 2020, **11**, 5449.

37 S. Park, M. H. Lee, K. S. Ahn, H. H. Choi, J. Shin, J. Xu, J. Mei, K. Cho, Z. Bao, D. R. Lee, M. S. Kang and D. H. Kim, *Adv. Funct. Mater.*, 2016, **26**, 4627–4634.

38 H. Fang, Q. Chen, Y. Lin, X. Xu, J. Wang, M. Li, C. Xiao, C. R. McNeill, Z. Tang and Z. Lu, *Angew. Chem., Int. Ed.*, 2025, **137**, e202417951.

39 T. Lu and Q. Chen, *Chem.: Methods*, 2021, **1**, 231–239.

40 Y. Xie, J. Tian, X. Yang, J. Chen, S. Yu, D. Tang, X. Hu, Y. Sun and M. Lv, *Adv. Mater.*, 2025, **37**, e02485.

41 Z. Wu, C. Sun, S. Dong, X. F. Jiang, S. Wu, H. Wu, H. L. Yip, F. Huang and Y. Cao, *J. Am. Chem. Soc.*, 2016, **138**, 2004–2013.

42 Y. Wang, J. Wen, Z. Shang, Y. Zhong, H. Zhang, W. Liu, W. Han, H. Yang, J. Liu, J. Zhang, H. Li and Y. Liu, *Angew. Chem., Int. Ed.*, 2025, **137**, e202506252.

43 R. Yu, X. Wei, G. Wu, T. Zhang, Y. Gong, B. Zhao, J. Hou, C. Yang and Z. A. Tan, *Energy Environ. Sci.*, 2022, **15**, 822–829.

44 G. Zhang, Q. Chen, Z. Zhang, J. Fang, C. Zhao, Y. Wei and W. Li, *Angew. Chem., Int. Ed.*, 2023, **62**, e202216304.

45 G. Zhang, Q. Chen, Z. Zhang, Z. Gao, C. Xiao, Y. Wei and W. Li, *Adv. Mater.*, 2023, **36**, 2310630.

46 L. Liu, Y. Kan, K. Gao, J. Wang, M. Zhao, H. Chen, C. Zhao, T. Jiu, A. K. Y. Jen and Y. Li, *Adv. Mater.*, 2020, **32**, 1907604.

This journal is © The Royal Society of Chemistry 2026

Energy Environ. Sci., 2026, **19**, 2237–2245 | **2245**